**PAPER • OPEN ACCESS**

# Generation and characterisation of few-pulse attosecond pulse trains at 100 kHz repetition rate

To cite this article: Mikhail Osolodkov *et al* 2020 *J. Phys. B: At. Mol. Opt. Phys.* **53** 194003

View the article online for updates and enhancements.

# Generation and characterisation of few-pulse attosecond pulse trains at 100 kHz repetition rate

**Mikhail Osolodkov**[1] ⊙**, Federico J Furch**[1] ⊙**, Felix Schell**[1]**, Peter Šušnjar**[1]**, Fabio Cavalcante**[2]**, Carmen S Menoni**[2]**, Claus P Schulz**[1]**, Tobias Witting**[1,3] ⊙ **and Marc J J Vrakking**[1]

[1] Max Born Institute for Nonlinear Optics and Short Pulse Spectroscopy, Max-Born-Straße 2a, 12489 Berlin, Germany
[2] Department of Electrical and Computer Engineering, Colorado State University, Fort Collins, CO 80523, United States of America

E-mail: witting@mbi-berlin.de

## Abstract

The development of attosecond pump–probe experiments at high repetition rate requires the development of novel attosecond sources maintaining a sufficient number of photons per pulse. We use 7 fs, 800 nm pulses from a non-collinear optical parametric chirped pulse amplification laser system to generate few-pulse attosecond pulse trains (APTs) with a flux of $>10^6$ photons per shot in the extreme ultraviolet at a repetition rate of 100 kHz. The pulse trains have been fully characterised by recording frequency-resolved optical gating for complete reconstruction of attosecond bursts (FROG-CRAB) traces with a velocity map imaging spectrometer. For the pulse retrieval from the FROG-CRAB trace a new ensemble retrieval algorithm has been employed that enables the reconstruction of the shape of the APTs in the presence of carrier envelope phase fluctuations of the few-cycle laser system.

Keywords: attosecond pulse generation, optical parametric amplification, attosecond pulse characterisation

(Some figures may appear in colour only in the online journal)

## 1. Introduction

High energy near infrared (NIR) pulses with durations on the femtosecond timescale allow the generation of attosecond pulses in the extreme ultraviolet (XUV) through the process of high-order harmonic generation (HHG) [1]. Combined with a phase-locked replica of the NIR pulses in a pump–probe configuration, attosecond XUV pulses can be used for attosecond timescale spectroscopy experiments [2]. The process under

investigation can be studied by measuring the absorption of the attosecond pulse or by detecting momentum distributions of photoelectrons or ions resulting from the interaction of the sample with a sequence of laser pulses. A more sophisticated approach than the latter is the coincident detection of all charged particles resulting from the interaction utilizing reaction microscopes or COLTRIMS (cold target recoil ion momentum spectroscopy) detectors [3]. Measurements of the correlated three-dimensional momentum distributions of all charged particles resulting from the interaction in coincidence provides access to the photoelectron momentum distributions in the recoil frame in the case of a dissociating molecule. Previously applied to strong field ionization experiments [4, 5], the combination of attosecond pump–probe spectroscopy with coincidence detection [6] permitted spatio-temporal

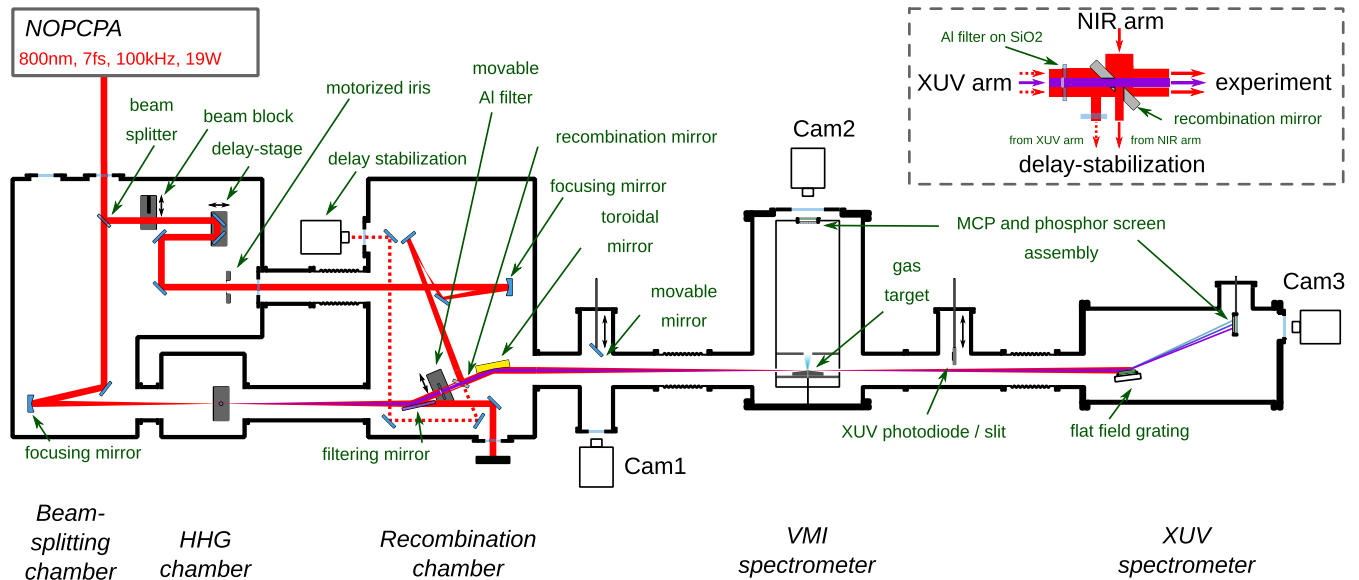J. Phys. B: At. Mol. Opt. Phys. **53** (2020) 194003

M Osolodkov *et al*



**Figure 1.** Schematic top view of the experimental setup. The NIR and XUV beams are shown in red and violet respectively. Inset: schematic view of the recombination mirror. For a detailed description we refer to the text.

reconstruction of the photoionization process in a CO molecule [7], and has been used to characterise the influence of coupled electron–nuclear dynamics during the dissociative ionization of $H_2$ molecules [8].

In order to perform coincident many-particle detection, at most one atom or molecule should be ionised per laser shot. On the other hand, the number of detected events should be high enough to achieve good statistics. Together these two conditions result in the demand for high repetition rate laser systems with a sufficiently high pulse energy to drive the HHG process. In recent years significant development of high repetition rate ($\gg$10 kHz) high energy laser sources enabled XUV generation at high repetition rates [9–14]. So far, with the exception of [15, 16], who reported RABBITT experiments at 100 kHz using a fibre laser post-compressed to 40 fs, no pump–probe experiments or pulse characterisation were reported. In particular, there have not been any reports yet demonstrating the complete characterisation of attosecond pulses generated using a high repetition rate few-cycle non-collinear optical parametric chirped pulse amplification (NOPCPA) driver, which is important given concerns that NOPCPA laser systems can suffer from spatio-temporal couplings. We have carefully modelled [17] and experimentally characterised and optimised [18] the spatio-temporal couplings of the laser system used in the current paper leading to a situation where they are not expected to have a detrimental effect on the HHG [10]. In this letter we report on the generation and characterisation of few-pulse XUV attosecond pulse trains (APTs) in the 15 to 40 eV energy range with a flux of $>10^6$ photons per shot at a repetition rate of 100 kHz. The APTs are accompanied by phase-locked <10 fs NIR pulses in order to enable pump–probe experiments.

In the NOPCPA system the carrier envelope phase (CEP) is stabilised by a fast feedback loop that stabilises CEP variations in the oscillator and a slow loop that corrects for CEP drifts in the amplifier. During the white light

generation inside the f-to-2f interferometer of the slow loop, the laser's shot-to-shot pulse energy fluctuations of 2% would lead to an added CEP noise of 320 mrad due to amplitude-to-phase coupling [19]. Therefore, during the experiment the slow loop was deactivated. As a result the experiments were performed with few-cycle pulses with a slowly varying CEP. The changing CEP of the driving NIR laser will lead to corresponding variations of the structure of the APT. Therefore the frequency-resolved optical gating for complete reconstruction of attosecond bursts (FROG-CRAB) trace encodes the properties of both an ensemble of NIR pulses and their corresponding APTs. In order to extract the temporal profile of the fluctuating APTs and the short NIR pulses (with fluctuating CEP), we apply the time-domain ensemble extended ptychographic iterative engine (td-e$^2$ PIE) that we have recently introduced and that is presented in our companion paper 'retrieval of attosecond pulse ensembles from streaking experiments using mixed state time-domain ptychography', which is also part of the present special issue [20].

## 2. Experimental setup

A sketch of the experimental setup is shown in figure 1. The NOPCPA system delivers up to 190 $\mu$J, 7 fs pulses centred at 800 nm with a repetition rate of 100 kHz [18, 21]. The attosecond pump–probe setup consists of three separate interconnected vacuum chambers. In the beam-splitting chamber the s-polarized NIR pulses from the NOPCPA system are split into two beams with an 80/20 ratio using a beam splitter with a flat response over the spectral range 500–1100 nm. The more intense of the two beams is transmitted by the beam splitter and then used for the generation of high-order harmonics. In what follows we are going to refer to this arm of the interferometer as the XUV arm and to the other one as the NIR arm. In the beam-splitting chamber the NIR beam in
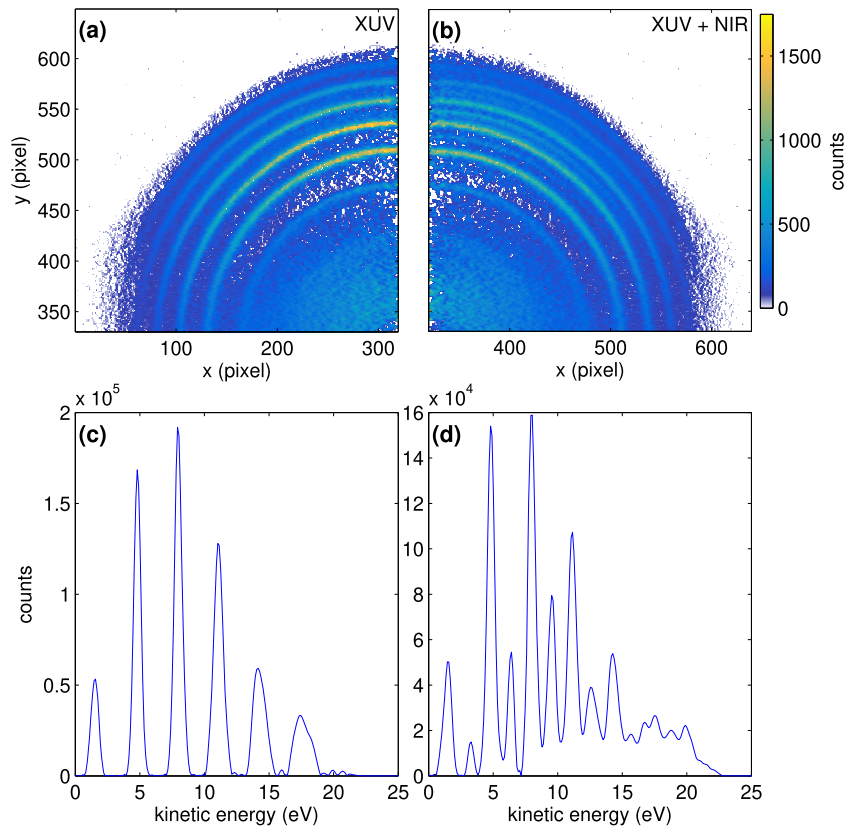
**Figure 2.** Examples of inverted VMI images and resulting photoelectron energy spectra. (a) XUV only VMI image, (b) VMI image with the XUV and NIR pulses at temporal overlap. In (b) the NIR field-induced sidebands are visible. The laser polarization axis is parallel to *y*. (c) Energy calibrated photoelectron spectrum XUV only; (d) photoelectron spectrum where XUV and NIR pulses overlap. The sidebands are clearly visible between the photolines of the harmonics. The cut-off region shows a more complex modulation structure.

the XUV arm is focussed by a spherical mirror ($f = 50$ cm) into a 2 mm long gas cell positioned inside the HHG chamber. The NIR pulse compression is optimized for efficient HHG. The NIR peak intensity in the focus is estimated to be $2 \times 10^{14}$ W cm$^{-2}$. After HHG the high power NIR beam co-propagating with the XUV beam is filtered out in two steps in the recombination chamber. First, the two-color beam is reflected by a specially designed dichroic mirror. This mirror has a $Ta_2O_5/SiO_2$ broadband antireflection (AR) coating topped by a 200 nm thick layer of $SiO_2$. The AR coating is suitable for both s- and p-polarisation of the NIR beam. At a grazing incidence angle of 75 degrees the coating reflects the XUV beam with an average reflectivity of 45% in the 20–60 eV spectral range whereas only 20% of the NIR light is reflected, independent of the polarization. The remainder of the NIR beam is transmitted by the filtering mirror and sent to an external beam dump. In the second filtering step the remaining NIR radiation is blocked by a 200 nm thick aluminium filter mounted on a drilled 1 mm thick fused silica plate. In the NIR arm of the interferometer, a translation stage with nanometer precision (SmarAct SLC-175S-HV) is used to control the delay of the two pulses propagating in the two arms of the interferometer. A motorized iris (SmarAct SID-5714) installed in the NIR arm is used to control the NIR intensity delivered to the experiment. The beams from the XUV and NIR arms are recombined utilising a recombination mirror shown

schematically in the inset of figure 1. The recombination mirror has two 5 mm diameter drilled holes oriented at 90 degrees with respect to each other and at 45 degrees to the mirror surface. The size of the clear aperture of the Al filter is the same as the size of the holes in the recombination mirror. The XUV beam transmitted through the Al filter propagates through one of the holes in the mirror. Part of the NIR beam from the NIR arm is reflected on the recombination mirror around the hole, resulting in an annular beam that is then recombined with the XUV beam and co-propagates towards the experiment. In the NIR arm we generate a focus in a plane that is equivalent to the plane of the HHG target. A gold-coated toroidal mirror forms a 1:1 image (object distance 1250 mm) of the two planes in the interaction region of the detection system, ensuring that the NIR focus overlaps with the image of the XUV source.

To enable attosecond pump–probe experiments the XUV and NIR laser pulses need to have a stable relative time-delay. We use a combination of passive and active stabilisation schemes. The entire interferometer is built inside a vacuum system onto optical breadboards connected to an optical table and isolated from the vacuum chambers by bellows. The chambers themselves are vibration-isolated from the optical table. For active stabilisation the second output port of the recombination mirror is used. The beam layout is sketched in the inset of figure 1. The central part of the NIR beam from the NIR
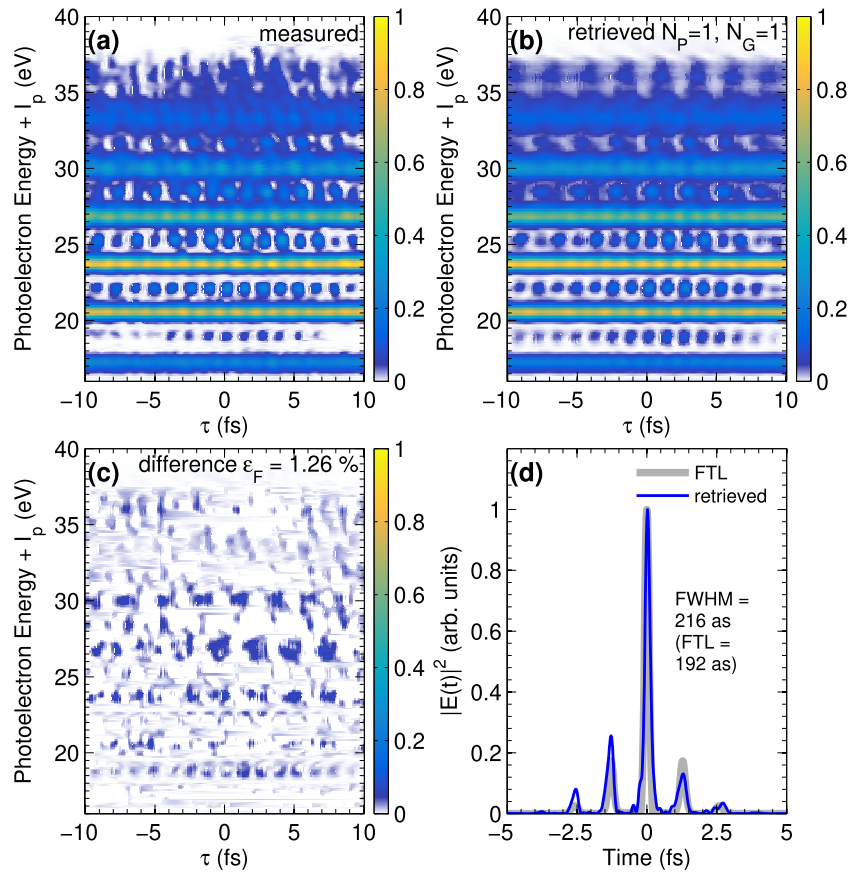
**Figure 3.** Retrieval of the XUV pulse train using a single pulse algorithm. (a) Measured trace. (b) Retrieved trace. (c) Difference map. (d) Retrieved intensity envelope $|E_{\mathrm{XUV}}(t)|^2$ of the XUV APT (blue line) compared to the Fourier limit (grey line). Note the periodic structures in the difference map (c) and the high FROG-error, which both indicate that the retrieved trace differs significantly from the measured trace.

arm of the interferometer propagates through the second hole in the recombination mirror and interferes with NIR radiation from the XUV arm that passes around the Al filter. This annular beam is reflected by the back-side of the recombination mirror and then used together with the transmitted part from the NIR arm for delay-stabilisation. We intentionally unbalance the glass amount in the two NIR beams (see inset figure 1) to introduce a time-delay between the two NIR beams (from the NIR and the XUV arm) of $\tau \approx 500$ fs. The resulting spectral interference fringes carry a $\cos(\Delta\phi + \omega\tau)$ modulation, where $\omega$ is the angular frequency of the laser, and $\Delta\phi$ is a phase-shift that is proportional to the path length difference between the two arms, and to be determined. The interference fringes are recorded by a home-made spectrometer which is equipped with a fast USB3 camera (Basler acA2040-90umNIR). The phase-shift is evaluated by a PC with a fast Fourier transform-based algorithm and a feedback signal is created controlling the delay-stage in the NIR arm of the interferometer. Using a small region of interest on the camera chip we reach acquisition loop speeds of up to 1 kHz. However, we restrict the driving speed of the piezo stage to <250 Hz to avoid resonances. This way pump–probe scans over 100 s of fs can be performed with attosecond phase-lock. The delay stability is around 50 as rms over hours of operation of the setup.

After the recombination chamber, the overlapping XUV and NIR pulses are focussed onto a gas target in a

velocity map imaging spectrometer (VMI). The sample atoms are ionised by the XUV beam in the presence of the NIR field and the resulting three-dimensional photoelectron momentum distributions are projected onto a two-dimensional detector (micro channel plate (MCP) and phosphor screen assembly) by a set of two electrodes forming an electrostatic lens. A 50 $\mu$m nozzle creating the gas target is incorporated into the repeller electrode of the VMI in order to increase the gas density in the interaction region [22]. The signal on the MCP and phosphor screen assembly is recorded using a complementary metal–oxide–semiconductor camera (Basler acA2040-90umNIR). An XUV spectrometer is positioned behind the VMI chamber. It allows detection of the spatially resolved XUV spectrum during the experiment. The XUV spectrometer consists of a flat field grating (Hitachi) mounted on a motorized stage and an MCP and phosphor screen assembly detector. The signal on the detector is imaged by a charge-coupled device camera (BASLER scA1400-17gm) installed outside of the vacuum chamber.

The XUV photon flux available for experiments was measured using an XUV photodiode (Opto diode AXUV100G) installed on a movable mount between the VMI and XUV spectrometer. The pump–probe measurements were performed with 70 mbar of krypton in the HHG gas cell. We measured an XUV photon flux of $2.2 \times 10^{11}$ photons/s, or $2.2 \times 10^6$ photons/shot in the interaction region of the
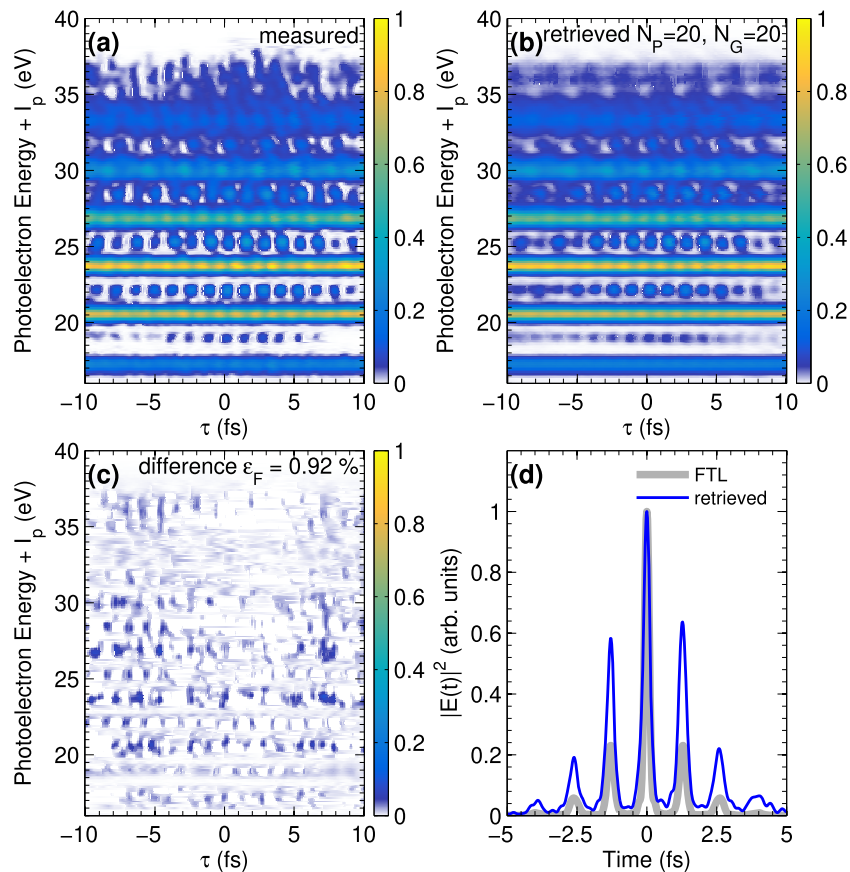
**Figure 4.** Retrieval of the XUV pulse train using the td-e$^2$ PIE algorithm. (a) Measured trace. (b) Retrieved trace. (c) Difference map.
(d) Mean of the retrieved intensity envelopes $|E_{\mathrm{XUV},k}(t)|^2$ of the XUV APTs (blue line) compared to their mean Fourier limit (grey line).
Please note the improvement of the difference map and the FROG-error compared to figure 3(c).

experiment. Considering the losses of the Al filter, the toroidal mirror, and the filtering mirror this corresponds to a flux of $1.5 \times 10^{12}$ photons/s after generation.

## 3. Results

For the attosecond pulse characterisation argon was used as target gas. The Ar atoms were ionized by XUV single photon absorption in the presence of an NIR laser pulse with an intensity of $5 \times 10^{10}\,\mathrm{W\,cm^{-2}}$. Since the three-dimensional photoelectron momentum distributions have cylindrical symmetry along the laser polarisation axis (along $\mathrm{p}_y$ in figure 2) they can be unambiguously retrieved from two-dimensional projections on a plane parallel to the axis of symmetry using an Abel inversion. VMI images were acquired for a pump–probe delay range of several 10 s of fs with 100 as steps. Figure 2 shows examples of inverted VMI images. In figure 2(a) we show the top left quadrant of an XUV-only image, and in (b) the top right quadrant of a measurement at temporal overlap of the NIR and XUV pulses. The NIR field-induced sidebands are clearly visible between the photoelectron rings from ionisation by the individual harmonics.

The photoelectron momentum distributions were integrated over an area from 0 to 10 degree with respect to the laser polarisation axis. Under these conditions the VMI

has an energy resolution $\Delta E/E$ of 1.5%. From the angularly integrated photoelectron momentum distributions we construct a spectrogram of photoelectron kinetic energy distributions as a function of the delay between the NIR and XUV pulses (shown in both figures 3(a) and 4(a)). The energy axis in figures 3 and 4 corresponds to the sum of the photoelectron kinetic energy and the ionisation potential of argon (15.76 eV), and therefore corresponds to the photon energy of the XUV pulses. From the photoelectron kinetic energy spectrograms both the XUV and NIR pulses can be reconstructed. As our 7 fs long NIR pulses generate APTs with only a few attosecond pulses, we are in a regime between long-pulse RABBITT, where one can assume a periodic APT, and streaking with isolated attosecond pulses. In long-pulse RABBITT the intensity of two-colour sidebands oscillates with a period that is half the period of the NIR pulse, i.e. the frequency of the sideband oscillations is $2\omega$. By contrast, in the streaking regime, the ponderomotive acceleration of the photoelectrons under the influence of the NIR streaking field leads to a periodicity of $1\omega$ in all observables. The spectrogram in figure 3(a) contains both $2\omega$ and $1\omega$ signal oscillations. The structure and strength of the $2\omega$ and $1\omega$ modulations are dependent on the photoelectron kinetic energy (i.e. the XUV photon energy). At low energy the APT contains a series of attosecond pulses leading to conventional RABBITT-like oscillations (dominant $2\omega$ component). Conversely, towards the cut-off of

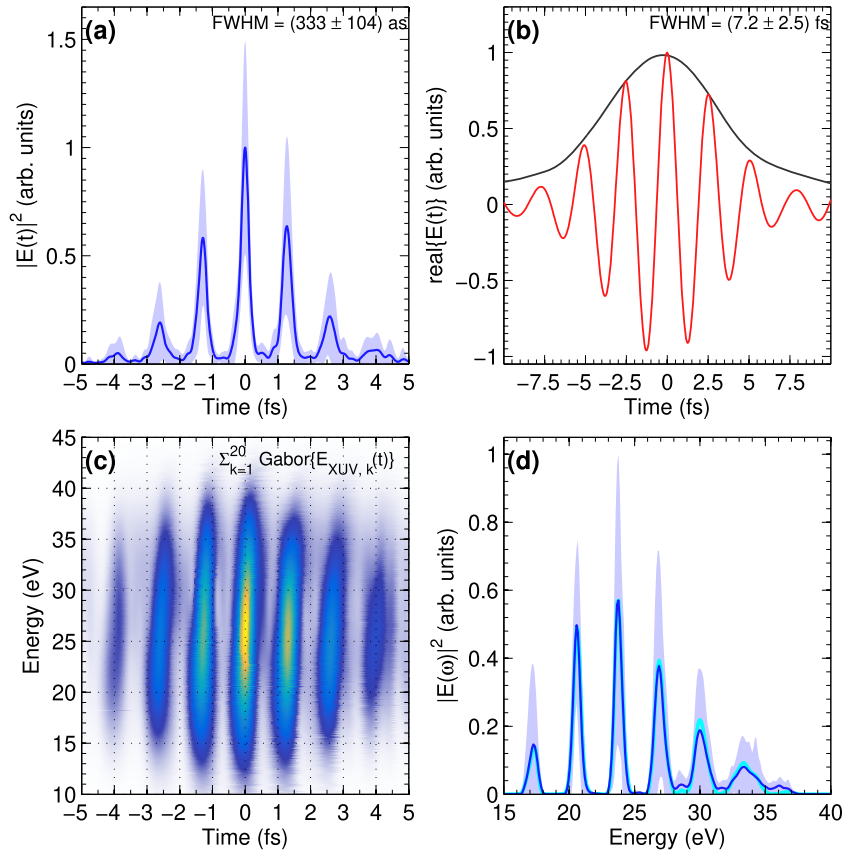J. Phys. B: At. Mol. Opt. Phys. **53** (2020) 194003

M Osolodkov *et al*



**Figure 5.** Details of the ensemble retrieval presented in figure 4(a) Mean retrieved XUV pulse intensity envelope (dark blue line). The standard deviation of the ensemble ($\pm 1\sigma$) is indicated by the light blue area. (b) Mean retrieved NIR pulse envelope (black line) and electric field (red line). (c) Sum of the Gabor distributions $\Sigma_k \text{Gabor}\{E_{\text{XUV}}\}$ of all pulses in the XUV ensemble. The slight atto-chirp is visible as a tilt in the Gabor plot. (d) Retrieved spectra of the XUV pulses. The mean is shown as dark blue line, the standard deviation $\pm 1\sigma$ as a light blue area. The variation of the harmonic peaks is greater near the cut-off. The retrieved spectrum agrees well this the measured XUV only spectrum (cyan line).

the high harmonic spectrum, the APT approaches an isolated attosecond pulse, and therefore the harmonic and sideband signals are modulated in a streaking-like manner (significant $1\omega$ component). Therefore, an RABBITT-type analysis consisting of fitting the sideband oscillations is not appropriate in our case.

In order to retrieve the XUV and NIR pulses, we employ a time-domain ptychography algorithm [23–25]. This iterative algorithm enables the reconstruction of the complex electric fields of both the unknown XUV and the dressing NIR pulses. It was demonstrated to be more robust and converging faster than other well-known reconstruction algorithms, such as principal component generalized projections algorithm or least squares generalized projections algorithm [24]. We run the time-domain ptychography algorithm in its extended ptychographic iterative engine (ePIE) implementation [24, 25]. Importantly, in the measurements shown here the CEP of the driving laser was not fully stabilised. Therefore the measured spectrograms are essentially sampling a distribution of NIR pulses with varying CEPs and also a distribution of varying APTs. The measured FROG-CRAB trace is therefore an incoherent sum of individual traces created by the members of two NIR and XUV pulse ensembles. Crucially, these NIR and XUV pulses are not correctly retrieved if a standard 'single

pulse' algorithm is used. This is illustrated in figure 3, which shows the retrieval of the XUV pulse train using a single pulse time-domain ptychography algorithm. In this retrieval the time-delay axis was kept as acquired in the experiment with $\delta\tau = 0.1$ fs and the photoelectron spectra were re-sampled onto a $2^{12}$ pixel grid ($\delta\hbar\omega = 50$ meV). The retrieval algorithm retrieves the amplitudes and phases of the electron wavepacket from which we retrieve the complex electric field of the APT by subtracting the dipole transition phases [26]. The retrieved spectrogram is displayed in figure 3(b) and the retrieved APT in figure 3(d) shows a strong central spike with relatively small satellites. As we have generated our APTs directly via HHG without use of any gating method, there is no physical reason to expect such an 'isolated' attosecond pulse. Using a model based on the strong field approximation to simulate the HHG emission [27] we calculated the expected APT for 7 fs driving pulses. This pulse train consists of 7 individual attosecond bursts under a Gaussian envelope following the envelope of the driving pulse. Also taking into account the relatively large FROG-error of $\epsilon_F = 1.26\%$ (see difference map in figure 3(c)), we have to conclude that a single pulse algorithm does not correctly retrieve APTs when fluctuations are present in the CEP of the driving laser along with corresponding changes in the shape of the APTs. The retrieval of a nearly isolated

attosecond pulse by the single pulse algorithm is somewhat reminiscent to the coherent artifact in femtosecond metrology [28].

In order to take the CEP fluctuations of the driver laser and the corresponding variations of the APTs into account, we have developed a new ensemble retrieval algorithm based on a mixed state extension of time-domain ptychography. The algorithm is described in detail in [20] where it was tested on simulated data. Briefly, this new algorithm assumes that the experimental trace consists of an incoherent sum of individual traces. Instead of retrieving one single pair of attosecond pulse and gate, the new algorithm retrieves ensembles of NIR and XUV pulses. The retrieval results from our ensemble algorithm are shown in figures 4 and 5. Figure 4(b) shows the retrieved spectrogram for ensembles of 20 XUV and 20 NIR pulses. Now the FROG-error is reduced to 0.92% (see the difference map in figure 4(c)). Unlike the results shown in figure 3(d) the retrieved APTs now have larger and more numerous satellites (see the blue line in figure 4(d), which represents the mean of the retrieved APTs). This is reasonable given that we drive the HHG with a 7 fs NIR pulse.

More details about the retrieved pulse ensembles are shown in figure 5. The retrieved XUV pulses are shown in (a), and the retrieved NIR pulses in (b). The NIR pulses have an FWHM duration of $(7.2 \pm 2.5)$ fs, with a CEP range of $\sigma_{CEP} = 0.49\pi$ rad. The average XUV pulse intensity envelope is plotted as a dark blue line in figure 5(a), with the light blue area indicating the standard deviation $\pm 1\sigma$. The spectral intensity distributions of the XUV pulses are shown in figure 5(d). The mean spectrum is plotted as a dark blue line, and the light blue area indicates the standard deviation $\pm 1\sigma$ of all spectra in the 20 pulse ensemble. The variation is greatest near the cut-off, consistent with the well-known CEP dependence of cut-off harmonics. As additional consistency check of the pulse reconstruction the XUV spectrum retrieved by the algorithm (blue line) can be compared to the measured XUV only spectrum (cyan line) in figure 5(d). The agreement is excellent. In order to visualize the complex time-frequency structure of the APTs better, the sum of the Gabor distributions of the 20 pulses in the XUV pulse ensemble are shown in figure 5(c). The individual attosecond pulses in the APT carry a small positive linear chirp, which stems from uncompensated atto-chirp. This chirp could be compensated by increasing the thickness of the aluminium filter [29].

## 4. Conclusion

In conclusion, we have demonstrated the generation of APTs at 100 kHz repetition rate with a flux of $2.2 \times 10^6$ photons/pulse on target and we have temporally characterised these APTs using a laser-dressed photoionisation experiment and the reconstruction of measured FROG-CRAB traces using a td-e$^2$ PIE algorithm, which accounts for pulse-to-pulse CEP fluctuations of the few-cycle NIR driver laser and corresponding pulse-to-pulse variations of the generated APTs. Henceforth, the attosecond beamline reported here is going to be used for two-colour XUV-NIR pump–probe spectroscopy measurements with coincidence detection.

## ORCID iDs

Mikhail Osolodkov ⬡ https://orcid.org/0000-0002-8328-5579
Federico J Furch ⬡ https://orcid.org/0000-0002-8444-7162
Tobias Witting ⬡ https://orcid.org/0000-0002-2512-1840

## References

[1] Krausz F and Ivanov M 2009 *Rev. Mod. Phys.* **81** 163–234
[2] Lépine F, Ivanov M Y and Vrakking M J J 2014 *Nat. Photon.* **8** 195–204
[3] Ullrich J, Moshammer R, Dorn A, Dorner R, Schmidt L and Schmidt-Bocking H 2003 *Rep. Prog. Phys.* **66** 1463–545
[4] Feuerstein B *et al* 2001 *Phys. Rev. Lett.* **87** 043003
[5] Eremina E, Liu X, Rottke H, Sandner W, Schatzel M, Dreischuh A, Paulus G, HWalther M R and Ullrich J 2004 *Phys. Rev. Lett.* **92** 173001
[6] Sabbar M, Heuser S, Boge R, Lucchini M, Gallmann L, Cirelli C and Keller U 2014 *Rev. Sci. Instrum.* **85** 103113
[7] Vos J, Cattaneo L, Patchkovskii S, Zimmermann T, Cirelli C, Lucchini M, Kheifets A, Landsman A S and Keller U 2018 *Science* **360** 1326–30
[8] Cattaneo L *et al* 2018 *Nat. Phys.* **1** 733–38
[9] Hadrich S, Rothhardt J, Krebs M, Demmier S, Klenke A, Tunnermann A and Limpert J 2016 *J. Phys. B: At. Mol. Opt. Phys.* **49** 172002
[10] Harth A *et al* 2017 *J. Opt.* **20** 014007
[11] Gonzalez A I *et al* 2018 *J. Opt. Soc. Am.* B **35** A6–14
[12] Lorek E, Larsen E, Heyl C, Carlstrom S, Palecek D, Zigmantas D and Mauritsson J 2014 *Rev. Sci. Instrum.* **85** 123106
[13] Krebs M, Hadrich S, Demmler S, Rothhardt J, Zair A, Chipperfield L, Limpert J and Tunnermann A 2013 *Nat. Photon. Lett.* **7** 555–9
[14] Pupeikis J, Chevreuil P A, Bigler N, Gallmann L, Phillips C R and Keller U 2020 *Optica* **7** 168–71
[15] Hammerland D *et al* 2019 *J. Phys. B: At. Mol. Opt. Phys.* **52** 23LT01
[16] Hammerland D *et al* 2019 arXiv:1907.01219
[17] Giree A, Mero M, Arisholm G, Vrakking M J J and Furch F J 2017 *Opt. Express* **25** 3104–21
[18] Witting T, Furch F J and Vrakking M J 2018 *J. Opt.* **20** 044003
[19] Li C, Moon E, Wang H, Mashiko H, Nakamura C M, Tackett J and Chang Z 2007 *Opt. Lett.* **32** 796–8
[20] Witting T, Furch F J, Kornilov O, Osolodkov M, Schulz C P and Vrakking M J J 2020 *J. Phys. B: At. Mol. Opt. Phys.* **53** 194001
[21] Furch F J, Witting T, Giree A, Luan C, Schell F, Arisholm G, Schulz C P and Vrakking M J 2017 *Opt. Lett.* **42** 2495–8
[22] Ghafur O, Siu W, Johnsson P, Kling M F, Drescher M and Vrakking M J 2009 *Rev. Sci. Instrum.* **80** 033110

[23] Spangenberg D, Rohwer E, Brügmann M H and Feurer T 2015 *Opt. Lett.* **40** 1002

[24] Lucchini M, Brugmann M H, Ludwig A, Gallmann L, Keller U and Feurer T 2015 *Opt. Express* **23** 29502–13

[25] Witting T, Greening D, Walke D, Matia-Hernando P, Barillot T, Marangos J and Tisch J 2016 *Opt. Lett.* **41** 4218–21

[26] Mauritsson J, Gaarde M B and Schafer K J 2005 *Phys. Rev.* A **72** 013401

[27] Lewenstein M, Balcou P, Ivanov M Y, L'Huillier A and Corkum P B 1994 *Phys. Rev.* A **49** 2117–32

[28] Fisher R A and Fleck J A 1969 *Appl. Phys. Lett.* **15** 287–90

[29] Lopez-Martens R *et al* 2005 *Phys. Rev. Lett.* **94** 33001